China Geology 6 (2023) 285−302

China Geology

Journal homepage: http://chinageology.cgs.cn
https://www.sciencedirect.com/journal/china-geology

Petrology, geochemistry and Ar-Ar geochronology of eclogites in Jinshajiang orogenic belt, Gonjo area, eastern Tibet and restriction on Paleo-Tethyan evolution

Yuan Tang[a,*], Ya-dong Qin[a], Xiao-dong Gong[a], Yong Li[a], Dong-bing Wang[a], Bao-di Wang[b]

[a] *Chengdu Center, China Geological Survey (Geosciences Innovation Center of Southwest China), Ministry of Natural Resources, Chengdu* 610081, *China*
[b] *China Aero Geophysical Survey and Remote Sensing Center for Natural Resources, Beijing* 100083, *China*

ARTICLE INFO

Article history:
Received 19 December 2022
Received in revised form 23 February 2023
Accepted 30 March 2023
Available online 6 April 2023

Keywords:
Eclogite
Ar-Ar geochronology
Closure of Paleo-Tethys ocean
Arc-continent collision
Geological survey engineering
Jinshajiang orogenic belt
Eastern Tibet

ABSTRACT

As one of the important Paleo-Tethys suture zones in eastern Tibet, the Jinshajiang orogenic belt is of great significance to study the tectonic evolution of the main suture zone of Paleo-Tethys. In this paper, eclogites developed in the Jinshajiang suture zone in Gonjo area, eastern Tibet, are selected as specific research objects, and petrological, geochemical and Ar-Ar geochronological analyses are carried out. The major element data of the whole rock reveals that the eclogite samples have the characteristics of picritic basalt-basalt and belong to the oceanic low potassium tholeiites. The results of rare earth elements and trace elements of the samples show that the protoliths of eclogites have characteristics similar to oceanic island basalt (OIB) or normal mid ocean ridge basalt (N-MORB). Muscovite (phengite) from two eclogite samples yield the Ar-Ar plateau ages of 247±2 Ma and 248±2 Ma respectively, representing the peak metamorphic age of eclogite facies and the timing of complete closure of the Jinshajiang Paleo-Tethys Ocean. Muscovite and biotite selected from the hosting rocks of eclogite yield the Ar-Ar plateau ages are 238±2 Ma and 225±2 Ma respectively, reflecting the exhumation age of eclogites and their hosting rocks. Combined with the zircon U-Pb dating data (244 Ma) of eclogites obtained in previous work, it can be concluded that the Jinshajiang Paleo-Tethys ocean was completely closed and arc-continent collision was initiated at about 248 –244 Ma (T_2^1). Subsequently, due to the large-scale arc (continent)-collision orogeny between Deqin-Weixi continental margin arc and Zhongza block (T_3^1–T_3^2), the eclogites were rapidly uplifted to the shallow crust.

1. Introduction

The Jinshajiang Paleo-Tethys orogenic belt in eastern Tibet has preserved a large amount of important information on deformation, metamorphism and magmatism related to the formation and spreading of the Paleo-Tethys, ocean-continent subduction, ocean closure and arc (continent)-continent collision and is an important window to study collision orogeny and plate tectonics. It is generally believed that the Jinshajiang Paleo-Tethys Ocean represents an ancient ocean basin that existed during the Devonian–Middle Triassic (D–T_2, Wang LQ et al., 1999; Sun XM and Jian P, 2004). However, there are different understandings about the timing of closure of the Jinshajiang Paleo-Tethys Ocean. On the basis of comprehensive study of regional data, Wu FY et al. (2020) inferred that all Paleo-Tethys (branch) Oceans, including the Jinshajiang Paleo-Tethys, had been closed in the late Permian (P_3), but did not provide specific evidence of this claim. According to the paleomagnetic research results, the closure time of the Jinshajiang Paleo-Tethys Ocean was no later than the late Triassic, which is obviously too broad and inaccurate (Song PP et al., 2015; Huang K and Opdyke ND, 2016; Yan YG et al., 2019; Guan C et al., 2021). Based on ophiolitic mélange zone unconformably covered by the late Triassic strata, the predecessors believed that the Jinshajiang Paleo-Tethys Ocean died out in the late Middle Triassic or Late Triassic (T_2/T_3; Wang LQ et al., 1999; Sun XM and Jian P, 2004). As a kind of special product of high-pressure metamorphism related to the subduction of plate, eclogite is considered to be a probe for the research on the physical and chemical processes in ocean-continent subduction-collision orogeny (Carswell DA and Harley SL, 1990; Yang JS et al., 2006, 2007; Zhai QG et al., 2011; Wang HN et al., 2018). The

* Corresponding author: *E-mail address*: tyvienna@163.com (Yuan Tang).

Literary editor: Xi-jie Chen
doi:10.31035/cg2023025
2096-5192/© 2023 China Geology Editorial Office.

newly discovered eclogite in the Gonjo area, eastern Tibet, is resulted from the closure of Jinshajiang Paleo-Tethys Ocean (Tang Y et al., 2020a, 2022a). In order to obtain more accurate evidence to reconstruct the Paleo-Tethyan evolution process in the Jinshajiang orogenic belt, the whole rock geochemical characteristics and Ar-Ar geochronology of eclogite have been carried out in this paper. Combined with the EMPA data and zircon U-Pb dating results obtained previously (Tang Y et al., 2020a), petrogenesis, exhumation process of eclogite and its tectonic significance are discussed in this paper.

2. Geological setting

2.1. Regional tectonic background

The Xijir-Ulan-Jinshajiang-Ailaoshan orogenic belt runs through Tibet, Qinghai, Sichuan and Yunnan provinces, extending from Yanghu and Guozacuo in northern Tibet through Xijir-Ulan Lake to Dengke-Yushu, southward through Batang, Derong-Benzilan-Diancang Mountain, turning southeastward through Ailao Mountain, and connecting with Song Ma orogenic belt in northern Vietnam (Wang XF et al., 2000; Pan GT et al., 2003; Metcalfe I, 2006; Jian P et al., 2008). According to the spatial distribution, it can be obviously divided into three sections: the Xijir-Ulan belt in the west, the Jinshajiang belt in the north and the Ailaoshan belt in the south (Liu ZQ et al., 1993; Zhong DL, 1998; Pan GT et al., 2003). The Jinshajiang orogenic belt, which is located in the "Three Parallel Rivers" area of eastern Tibet (Fig. 1a), together with the Lancangjiang and Nujiang orogenic belts, has attracted the attention of many geologists. The Jinshajiang orogenic belt is distributed in a north-south direction along the main rivers of the Jinshajiang, with a total length of about 710 km and a width of 2–30 km (Fig. 1b). The eastern side of this belt is Yidun arc and Zhongza block. The western side is close to the Jiangda-Deqin-Weixi continental margin arc, and then to the west is the Qamdo block (Figs. 1a, b; Liu ZQ et al., 1993; Wang LQ et al., 1999). To the north, it intersects with Ganzi-Litang tectonic belt in Dengke area (Fig. 1a; Xu et al., 2015).

The Jinshajiang suture zone in Gonjo area, eastern Tibet, is mainly comprised of a series of tectonic rock slices of different scales, lithology, and deformation degrees and strongly deformed matrix (Fig. 2). The rock slices are connected by many ductile-brittle/ductile faults that are nearly parallel to the suture zone. Therefore, the suture zone is present as a tectonic mélange belt. Tectonic slices mainly include: ultrabasic-basic rock (ΣPT_1op, $mvPT_1op$), marble (mbCPsli), marble+metamorphic basic rock (ges+$mbPT_1sc$), (retrograded) eclogite ($ehPT_1hpm$, $ecPT_1hpm$), metamorphic silica-limestone-argillaceous rock ($qsPT_1sa$), etc (Figs. 2, 3a). The matrix materials mainly consist of garnet bearing schist (*sch*+*Gr*PT_1) and garnet free schist or phyllite (*sch*PT_1), which are represented by garnet bearing plagioclase mica schist, garnet bearing mica quartz schist, plagioclase biotite schist, mica schist, biotite schist, biotite plagioclase schist containing red pillar and a small amount of phyllite.

Eclogites, the object of this study, are mainly distributed in the western margin of the Jinshajiang suture zone and hosted in the surrounding rock in the form of tectonic lenses (Fig. 3). The eclogite lenses vary in width from a few meters to more than ten meters. The hosting rocks of eclogite include serpentinized peridotite, diopside-tremolite marble, garnet-bearing biotite-muscovite-quartz schist, biotite-plagioclase gneiss, or carbonaceous mica schist (Tang Y et al., 2020a), which contact with eclogites in forms of fault or brittle-ductile shear zone (Figs. 3b, c). All these rocks have undergone retrograde metamorphism to different extents. The eclogites near the Luomai Village feature weak retrograde metamorphism. Therefore, they are fresh and well preserved (Fig. 3d). They occur in garnet-bearing plagioclase two mica schist and banded marble in the form of lens that is about 1–3 m wide (Fig. 3).

2.2. Petrological characteristics of eclogites

Based on textures and the modal proportions of main minerals, the eclogites in this zone can be divided into the following three types (Table 1): eclogite (D0521-1), garnet-albite-epidote-biotite actinolite schist (D0029, PM003-71, 19XS02, D0628 and D3037) and garnet-actinolite schist (21LM01).

The eclogite mainly consists of garnet, clinopyroxene, hornblende, biotite, quartz and a small amount of muscovite and rutile (Table 1, Figs. 4a, b). The garnets are quasi-equiaxial-xenomorphic granular in shape with a particle size of 0.6–2.6 mm in general. Radial cracks can be seen on the surface of garnets, and inclusions such as hornblende, quartz, rutile, muscovite and pyroxene are observed in several garnet grains. The clinopyroxenes are mainly in the shape of hypautomorphic columnar granules, with the grain size of 0.2–2.0 mm. They are distributed among garnet grains, arranged directionally, with cleavages similar to the ones of pyroxenes. According to the EMPA data, the clinopyroxene features high content of Na_2O (5.6%–6.0%) and corresponding jadeite (Jd) molecules of 37%–40%. Therefore, the clinopyroxenes are typical omphacites (Tang Y et al., 2020a). The hornblendes are also in the shape of hypautomorphic columnar granular, with grain size of 0.2–2 mm in general and 2–3 mm in small amount. They are generally distributed among garnet grains while a small number of them are embedded inside garnet grains. The biotites are flaky and foliaceous in shape, with a particle size of 0.2–1.6 mm in general. They are distributed among garnet grains. The muscovites develop in fine flakes. Some of them exist in the center of garnets, and some are distributed between garnets and omphacites. The EPMA data reveal that the muscovites are phengites (Tang Y et al., 2020a). The quartzs are xenomorphic granular in shape, with a particle size of 0.1–0.8 mm. They are scattered among garnet grains, reflecting that they were formed late and do not belong to the same generation minerals as the garnets and omphacites. The rutiles are hypidiomorphic-xenomorphic granular in shape,

with a particle size of 0.1–0.5 mm in general. They are mainly scattered among garnet grains, with a small part being distributed inside the grains of hornblendes, omphacites and garnets.

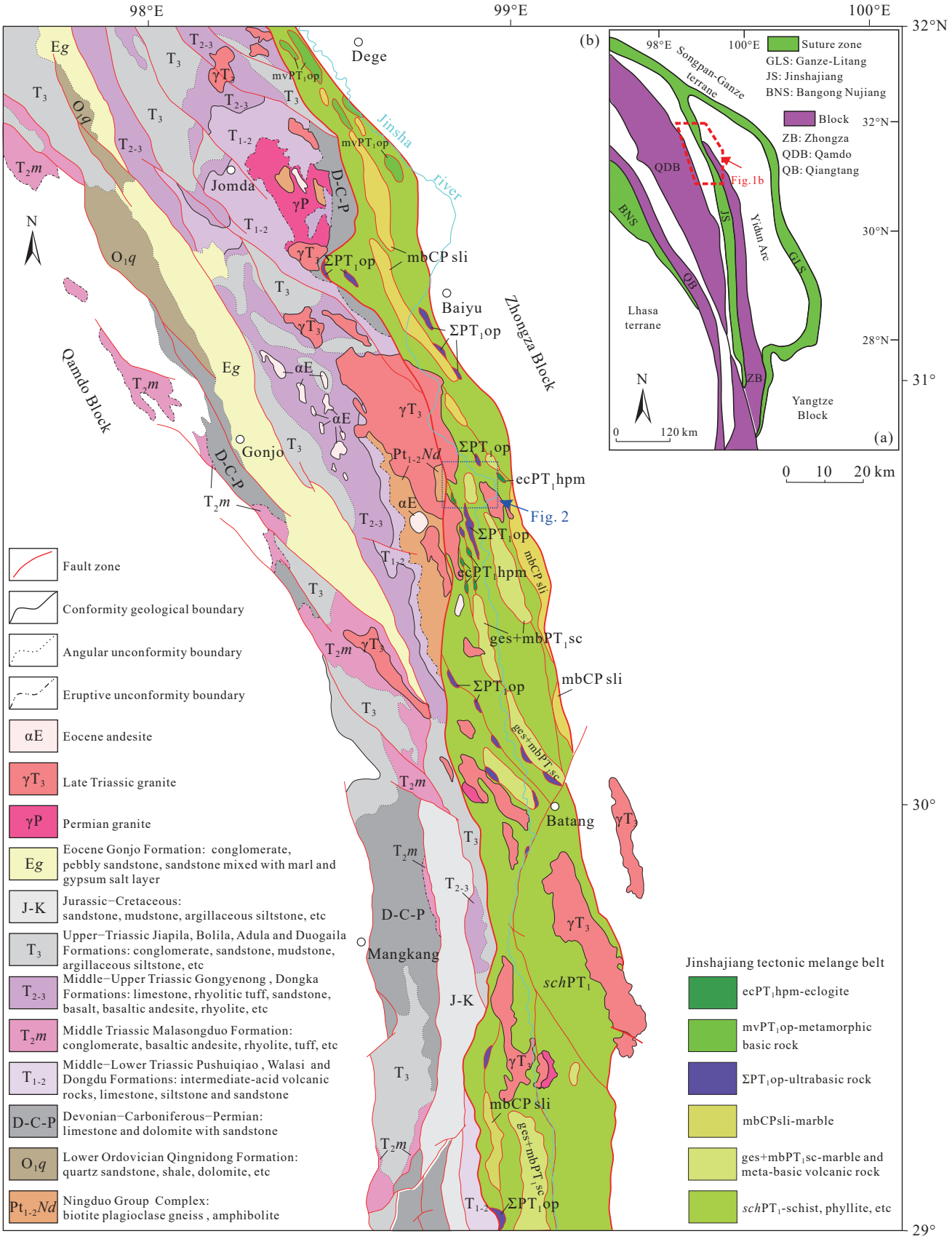

Fig. 1. a–Geotectonic position of the Jinshajiang orogenic belt (after Li XZ et al., 1999); b–geological sketch of Jinshajiang orogenic belt in eastern Tibet (location of the area shown in Fig. 1a).

The garnet-albite-epidote-biotite-actinolite schist consists of albite, actinolite, biotite, muscovite, epidote, residual garnet and sphene (Table 1, Fig.4c). Albites, actinolites, biotites and epidotes are mixed, and their aggregates are oriented distributed. The albites are xenomorphic granular in shape, with a general particle diameter of less than 0.6 mm. There are actinolites, biotites and sphenes embedded in the albite grains. The actinolites are thin-columnar, needle-columnar, fiber-columnar and granular in shape, with a diameter of less than 0.3 mm, showing light blue green and weak polychrome. The biotites are flaky-foliaceous, with the diameter of <0.2 mm. They are brown, with obvious polychrome, and are mostly chloritized. Muscovites are aslo flaky-foliaceous in shape, with a diameter of < 0.8 mm. Epidotes are in fine granular shape with particle size < 0.2 mm. The residual garnets are mainly quasi-equiaxial granular in shape, with a diameter of less than 2.0 mm and distributed in scattered form. There are sphenes embedded in the garnet grains. The rims of garnet particles were metasomatized by albite, biotite and epidote, and formed coronary reaction rims.

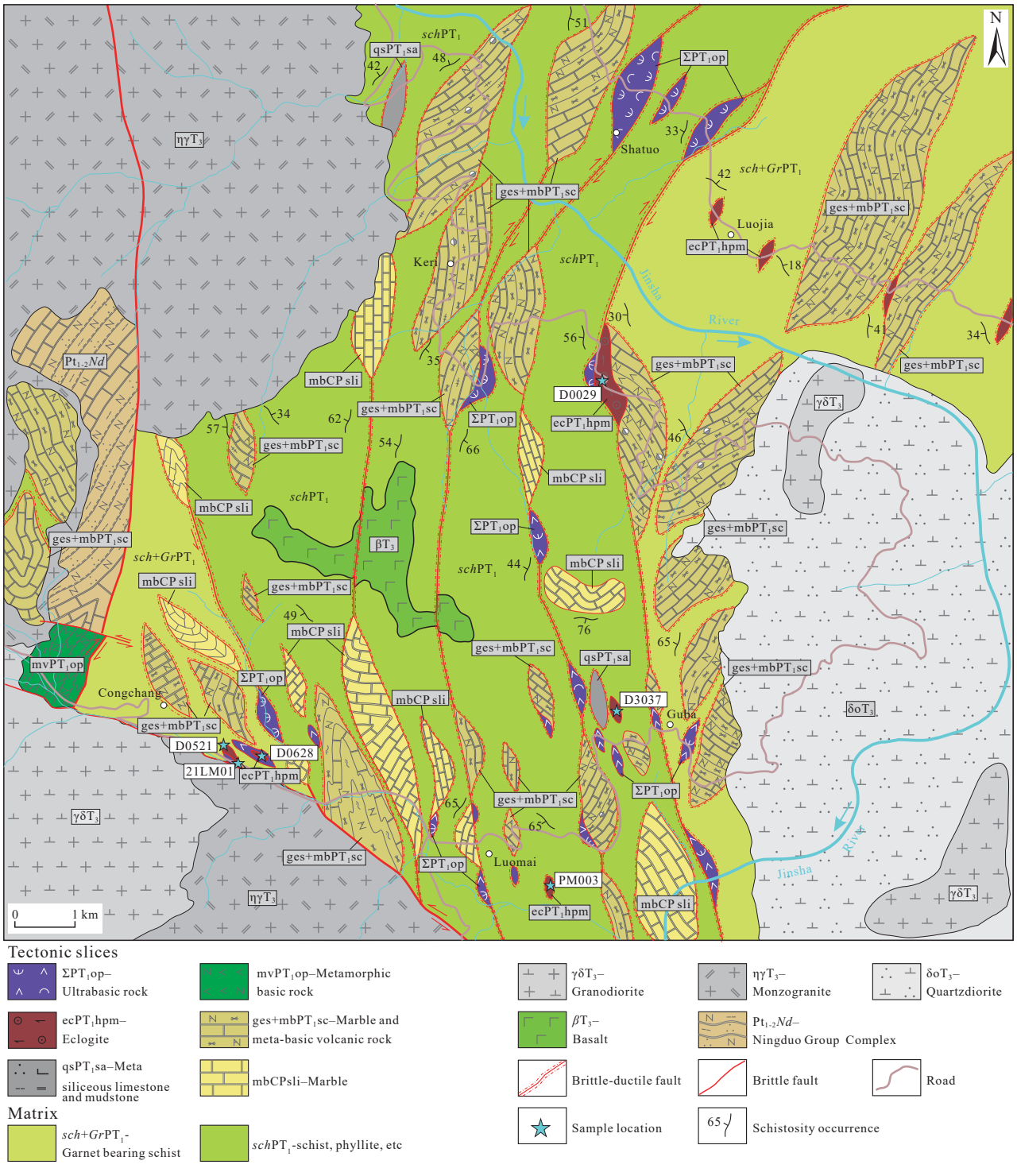

Fig. 2. Distribution characteristics of tectonic blocks in Jinshajiang suture zone, Gonjo County, Eastern Tibet (location shown in Fig. 1b).

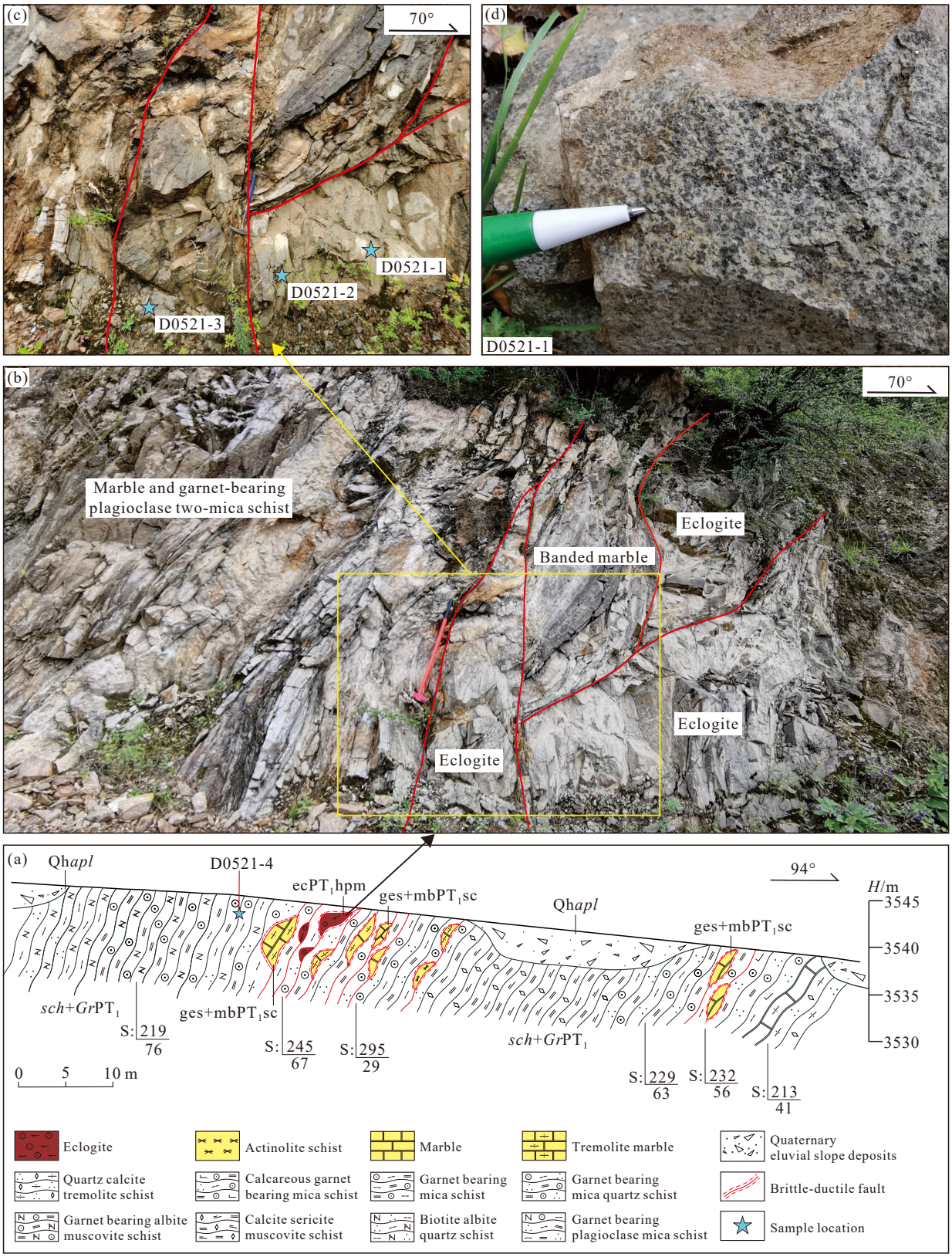

Fig. 3. a–Geological profile of eclogite and hosting rocks in Gonjo area; b and c–eclogites occurring in the shape of lens about 1–3 m wide, preserved in garnet-bearing plagioclase two-mica schist and banded marble; d–hand specimens of eclogite with low retrograde metamorphism. The bule stars show the location of samples.

Sphenes are in the form of fine particles, and their aggregates are mainly distributed in linear and scattered directionally.

Garnet actinolite schist is composed of actinolite, garnet, albite, biotite, clinopyroxene and a small amount of rutile and sphene (Table 1, Figs. 4e–f). The actinolites are in the shape of xenomorphic columnar, with the particle size of 0.5–1 mm in general and 1–2 mm in some cases. Some aggregates are distributed in stripes. Some aggregates are pseudo-pyroxene,

Table 1. Petrological characteristics of (retrograde) eclogites.

Lithology	Samples	Color, texture and structure	Mineralogy
Eclogite	D0521-1	Grayish-green, Medium-coarse granular blastic texture, Blocky structure	Garnet (45%–50%), omphacite (± 15%), hornblende (± 15%), biotite (5%–10%), muscovite (5%–10%), quartz (5%–10%), rutile (1%–5%)
Garnet bearing plagioclase mica schist (hosting rock)	D0521-4	Yellowish grey, Lepido-granular blastic texture, Schistose structure	Quartz (± 45%), plagioclase (10%–15%), biotite (10%–15%), muscovite (20%–25%), garnet (± 5%), calcite (1%–5%)
Garnet-albite-epidote-biotite actinolite schist	D0029, PM003-71, 19XS02, D0628, D3037	Greenish grey, Lepido-nemato-granular blastic texture, Oriented structure	Albite (30%–35%), actinolite (± 30%), epidote (5%–10%), biotite (5%–10%), muscovite (5%), residual garnet (± 15%), sphene (5%)
Garnet actinolite schist	21LM01	Green, Nemato- granular blastic texture, Blocky structure	Actinolite (50%–55%), garnet (± 25%), albite (± 10%), biotite (± 5%), omphacite (1%–5%); a small amount of rutile and sphene

indicating that actinolites may be formed by retrograded metamorphism of clinopyroxenes. Garnets are mainly hypautomorphic granular in shape, with particle size of 0.5–1 mm in general and 1–2 mm in a small amount. Garnets are slightly directionally arranged and metasomatized by actinolite, zoisite, epidote, calcite and biotite. Garnets are mainly almandine. Albites are hypautomorphic-xenomorphic granular in shape, with particle size of 0.5–1 mm in generale, and are scattered distributed. The biotites are flaky-foliaceous, with the diameter of 0.05–0.2mm. The clinopyroxenes are in the shape of xenomorphic columnar, with the particle size of 0.5–1 mm in general, and are metasomatized by actinolite, epidote, calcite and opaque minerals. They are in multiple colors, with Ng'= light green and Np'= colorless. The garnet actinolite schist is also formed due to the retrogressive metamorphism of the eclogite in the later stage.

The hosting rock of the eclogites is garnet-bearing plagioclase mica schist, consisting of quartz, plagioclase, muscovite, biotite, garnet and a small amount of calcite. Plagioclases are mainly xenomorphic granular in shape, with the particle size of 0.2–0.8 mm in general. They are distributed randomly or in a curved mosaic shape between grains. Plagioclases are obviously metasomatized by sericite, zoisite and carbonate rock. Quartzs are mainly in shape of xenomorphic granular with grain size of 0.2–0.8 mm. The quartz aggregates are relatively concentrated as lenses or stripes and arranged directionally. Undulatory extinction and sub-grains can be seen in some quartz grains. Both biotites and muscovites are flaky-foliaceous, with grain size of 0.2–1.0 mm. The aggregates are relatively enriched and distributed like lenses or stripes. Mica-fish can be seen locally, indicating that the rock was deformed by tectonism. The garnets are quasi-equiaxial-xenomorphic granular in shape with a particle size of 0.8–2.5 mm in general, and distributed unevenly. Cracks are visible on the garnet surface, mica is distributed along the cracks somewhere, and a little amount of quartz is embedded in some garnet grains locally.

3. Geochemical characteristics of retrograded eclogite

3.1. Analytical and Test Methods

Nineteen eclogite samples were collected for whole-rock major and trace element analyses. All samples of were cleaned of weathered surfaces prior to being powdered in an agate ring mill for subsequent major and trace element analyses at the Wuhan Sample Solution Analytical Technology Co., Ltd., Wuhan, China. Major element analyses of whole rock were conducted on XRF (Primus Ⅱ, Rigaku, Japan). The detailed sample-digesting procedure was as follows: (1) Sample powder (200 mesh) were placed in an oven at 105°C for drying of 12 hours; (2) ~1.0g dried sample was accurately weighted and placed in the ceramic crucible and then heated in a muffle furnace at 1000°C for 2 hours. After cooling to 400°C, this sample was placed in the drying vessel and weighted again in order to calculate the loss on ignition (LOI). (3) 0.6 g sample powder was mixed with 6.0 g cosolvent ($Li_2B_4O_7$: $LiBO_2$: LiF = 9 : 2 : 1) and 0.3 g oxidant (NH_4NO_3) in a Pt crucible, which was placed in the furnace at 1150°C for 14 mins. Then, this melting sample was quenched with air for 1 min to produce flat discs on the fire birck for the XRF analyses. Trace element analysis of whole rock were conducted on Agilent 7700e ICP-MS. The detailed sample-digesting procedure was as follows: (1) Sample powder (200 mesh) were placed in an oven at 105°C for drying of 12 hours; (2) 50 mg sample powder was accurately weighed and placed in a Teflon bomb; (3) 1 mL HNO_3 and 1 ml HF were slowly added into the Teflon bomb; (4) Teflon bomb was putted in a stainless steel pressure jacket and heated to 190°C in an oven for >24 hours; (5) After cooling, the Teflon bomb was opened and placed on a hotplate at 140°C and evaporated to incipient dryness, and then 1 mL HNO_3 was added and evaporated to dryness again; (6) 1 mL of HNO_3, 1 mL of MQ water and 1 mL internal standard solution of 10^{-6} In were added, and the Teflon bomb was resealed and placed in the oven at 190°C for >12 hours; (7) The final solution was transferred to a polyethylene bottle and diluted to 100 g by the addition of 2% HNO_3.

3.2. Results

The whole-rock major and trace elemental data for the analyzed samples are listed in Table 2. The eclogite samples have the characteristics of picritic basalt-basalt (Fig. 5a) with

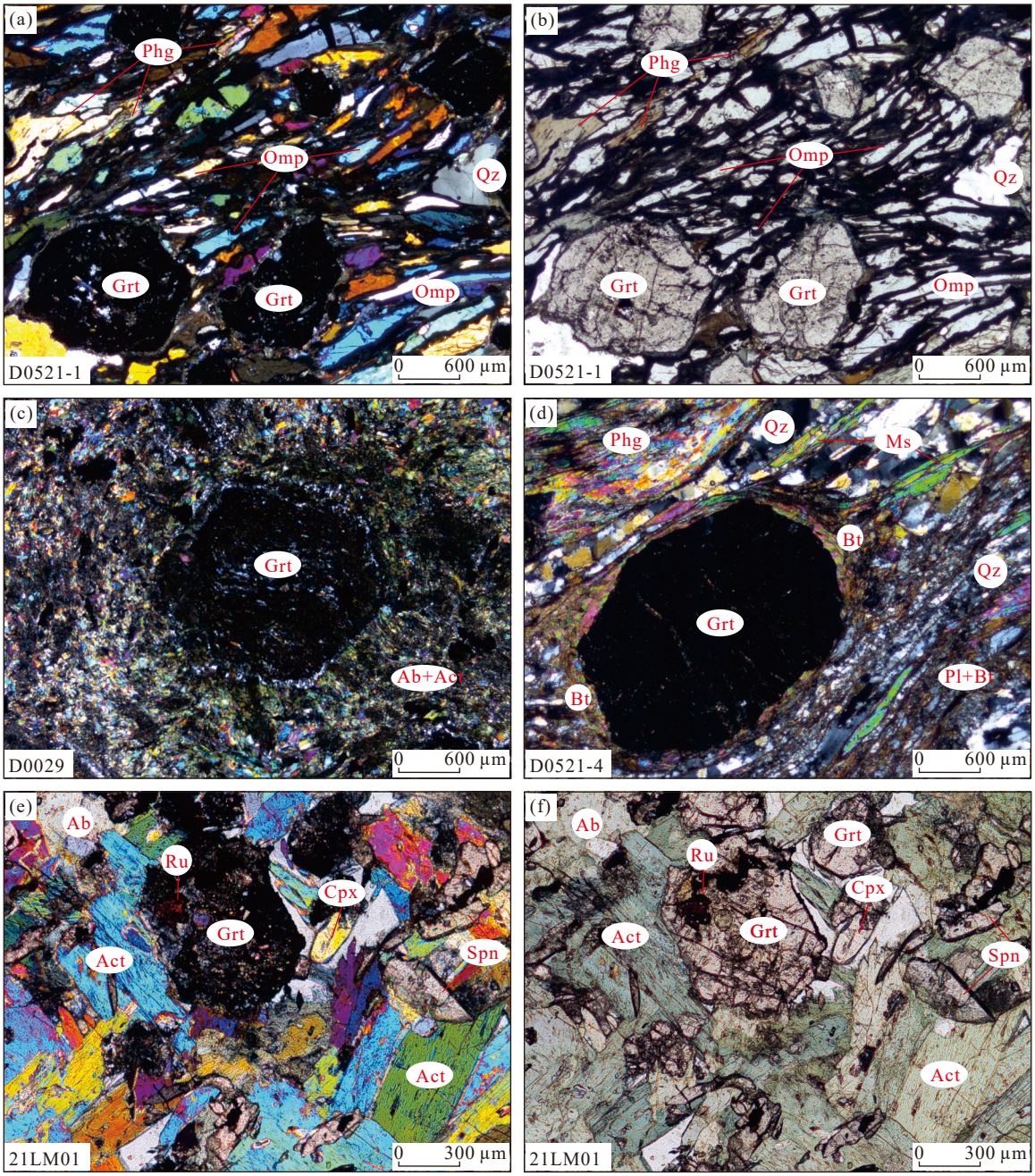

Fig. 4. Photomicrograph of eclogite (a, b, c, e, f) and hosting rock (d). Omp−omphacite; Grt−garnet; Qz−quartz; Phg−phengite; Cpx−clinopyroxene; Ab–albite; Act–actinolite; Pl−plagioclase; Bt−biotite; Ms−muscovite; Spn−Sphene; Ru−rutile; a, c, d and e −cross-polarized light; b and f−plane-polarized light.

SiO_2 contents ranging from 40.95% to 52.03%, and belong to the oceanic low potassium tholeiites based on the relatively low total alkali contents (Na_2O+K_2O) of 0.77%–4.97%. The contents of Al_2O_3 and CaO in these samples are relatively high, which are 11.58%–17.54% and 5.04%–14.61% respectively. The TiO_2 contents of these samples range from 0.77% to 5.02%, and the $Mg^{\#}$ is 35–69. On the SiO_2-FeO^t/MgO diagram, all of them plot in the tholeiitic field (Fig. 5b).

Chondrite-normalized REE patterns and Primitive-mantle normalized trace element for the eclogite samples are shown in Fig. 6. According to the total REEs contents and chondrite-normalized REE patterns, the eclogites can be divided into two groups. The samples of one group have high total REE concentrations (118×10^{-6}–287×10^{-6}), and they exhibit light rare earth element (LREEs) enrichment relative to the heavy rare earth elements (HREEs), with $(LREE/HREE)_N$=5.6–8.2 and $(La/Yb)_N$=6.05–12.58 (Fig. 6a; Sun SS and McDough WF, 1989). The curves of Chondrite-normalized REE pattern incline to the right, similar to the characteristics of oceanic island basalt (OIB). The chondrite normalized REE pattern for samples of the other group shows that LREEs are depleted and HREEs are flat ($(La/Yb)_N$=0.45–1.17, Fig. 6c; Sun SS and McDough WF, 1989), similar to the distribution pattern of N-MORB.

The primitive mantle-normalized spider diagrams also

Table 2. Major (%) and trace element composition of eclogites.

Sample	21LM01-1	21LM01-2	21LM01-3	21LM01-4	D0521-1	D0521-2	D0521-3	PM003-60	PM003-71	19XS02-1	19XS02-2	19XS02-3	D0029-1	D0029-2	D0628-1	D0628-2	D3037-1	D3037-2	D3037-3
SiO_2	40.75	40.47	41.18	41.16	46.45	46.94	46.82	47.67	45.83	43.64	43.77	44.42	48.07	50.78	46.37	45.71	49.84	49.77	49.95
TiO_2	4.32	4.96	4.63	4.58	2.79	2.61	2.75	2.36	2.23	2.28	2.76	1.86	1.13	0.76	1.84	1.93	1.51	1.55	1.46
Al_2O_3	13.22	12.83	12.90	12.91	14.53	13.97	14.42	14.10	13.79	14.14	16.57	10.5	13.30	16.53	14.87	15.08	15.26	15.45	15.77
TFe_2O_3	18.39	17.68	18.35	18.22	14.40	13.47	14.48	13.13	12.73	10.78	17.06	13.05	11.36	9.25	12.33	13.07	9.13	8.86	9.51
MnO	0.43	0.44	0.47	0.47	0.19	0.19	0.21	0.19	0.19	0.13	0.15	0.18	0.24	0.17	0.21	0.20	0.35	0.32	0.28
MgO	6.54	6.59	6.72	6.66	7.11	6.56	6.76	6.34	6.87	5.59	4.68	7.3	11.07	10.30	7.31	8.82	6.32	6.37	7.11
CaO	13.82	14.44	13.68	13.58	10.72	10.19	10.36	10.70	10.81	9.5	4.76	9.94	11.44	7.42	11.92	10.79	9.18	9.49	8.51
Na_2O	0.51	0.49	0.50	0.50	3.89	2.48	2.48	2.76	3.07	3.54	4.18	2.65	1.29	3.10	2.40	2.65	1.67	1.68	2.02
K_2O	0.28	0.32	0.27	0.27	1.81	0.86	0.74	0.86	0.70	0.78	0.13	0.51	0.51	0.30	0.26	0.40	2.44	2.32	2.83
P_2O_5	0.41	0.61	0.41	0.41	0.323	0.33	0.37	0.32	0.29	0.24	0.42	0.27	0.03	0.07	0.17	0.17	0.09	0.09	0.2
LOI	0.67	0.85	0.52	0.52	0.00	2.06	0.27	1.42	3.22	9.17	5.42	9.2	1.82	1.69	2.02	1.02	2.69	2.74	2.27
Total	99.33	99.66	99.63	99.27	102.21	99.64	99.65	99.84	99.74	99.79	99.90	99.88	100.25	100.37	99.70	99.84	98.47	98.63	99.91
$Mg^{\#}$	42	43	42	42	50	49	48	49	52	51	35	53	66	69	54	57	58	59	60
Na_2O+K_2O	0.80	0.81	0.77	0.78	3.47	3.42	3.24	3.67	3.91	4.77	4.56	3.48	1.83	3.45	2.73	3.08	4.29	4.17	4.97
Na_2O/K_2O	2	2	2	2	3	3	3	3	4	5	32	5	3	10	9	7	1	1	1
Li	4.81	4.89	5.16	5.27	15.9	14.5	11.0	12.3	26.7	16.7	16.5	10.3	14.2	13.3	17.6	19.5	11.6	13.2	15.8
Be	6.02	5.51	5.52	5.46	1.17	1.10	1.30	1.11	1.47	1.80	1.63	2.19	1.06	0.31	0.84	0.97	2.69	2.25	3.35
Sc	35.4	32.7	35.3	35.3	32.3	29.9	31.1	30.6	31.0	29.0	36.2	32.2	42.1	44.2	43.0	45.4	39.5	41.1	39.6
V	340	352	348	347	367	343	354	327	326	284	314	264	244	204	303	326	301	278	298
Cr	134	126	140	139	205	191	200	131	216	198	503	804	218	54.0	200	202	284	294	312
Co	47.5	50.1	45.6	45.4	48.4	46.1	46.9	40.6	40.9	46.7	90.1	128.0	45.5	42.8	48.7	48.4	39.4	42.3	40.0
Ni	116	141	140	141	115	116	110	100	130	100	225	613	157	68.5	112	119	124	128	117
Cu	68.4	47.4	74.2	73.3	155	154	130	152	111	164.0	148.0	183.0	51.6	23.4	39.6	65.5	70.3	100	35.9
Zn	91.5	94.9	93.9	93.2	119	107	111	97.6	106	114	234	118	115	67.8	97.2	102	248	233	262
Ga	12.1	11.3	11.7	11.5	21.1	21.3	21.2	20.1	21.0	23.6	30.3	20.0	14.0	15.9	18.2	19.5	14.1	14.3	14.2
Rb	5.32	7.13	5.84	5.88	24.8	25.1	21.8	24.9	28.3	32.3	4.79	19.9	15.8	9.17	6.49	8.23	63.7	57.3	91.6
Sr	163	166	130	129	282	342	293	82.8	187	822	456	444	308	182	173	197	112	133	102
Y	44.3	43.2	45.1	44.8	32.3	30.2	31.7	29.9	27.8	18.4	27.8	18.5	28.7	19.3	44.3	44.9	36.4	35.9	36.1
Zr	190	181	200	190	180	163	176	169	151	175	270	165	87.5	44.9	133	129	128	132	126
Nb	40.0	42.2	42.0	42.0	23.9	21.8	23.3	20.9	18.5	24.4	41.7	20.9	3.00	0.78	2.89	3.20	5.39	5.19	4.97
Sn	3.04	3.94	3.43	3.36	1.48	1.53	1.49	1.33	1.13	1.76	2.37	1.44	1.07	0.59	1.36	1.67	1.82	1.91	1.54
Cs	0.84	1.38	2.21	2.17	1.63	5.38	1.58	2.01	2.59	5.10	0.46	2.97	2.06	1.59	0.60	1.35	2.61	2.27	3.10
Ba	52.7	59.5	55.1	54.7	262	323	253	203	232	1140	150	516	115	60.8	76.1	65.6	577	567	797
La	32.5	47.5	34.7	34.5	26.5	22.9	23.8	23.7	20.4	26.8	38.5	22.1	3.08	1.33	4.94	4.85	4.75	4.52	6.26
Ce	79.3	113	86.2	85.7	58.7	50.9	53.1	50.8	44.7	53.4	75.9	44.5	9.12	4.39	15.6	15.6	12.8	12.7	15.8
Pr	10.6	14.4	11.4	11.4	7.56	6.59	6.78	6.51	5.66	6.76	9.61	5.59	1.59	0.84	2.61	2.64	2.32	2.22	2.68
Nd	46.1	62.6	50.3	50.3	32.7	28.4	29.5	28.1	25.7	27.8	38.8	23.6	8.34	4.83	14.2	14.5	12.2	12.2	13.9
Sm	9.76	12.5	10.6	10.7	7.33	6.81	7.15	5.86	5.42	5.66	7.56	4.91	2.99	1.89	4.64	4.59	3.67	3.56	4.33
Eu	3.57	4.33	3.79	3.75	2.26	2.11	2.19	1.97	1.85	2.12	2.65	1.75	1.23	1.02	1.66	1.65	1.21	1.32	1.62

Table 2. (*Continued*)

Sample	21LM01-1	21LM01-2	21LM01-3	21LM01-4	D0521-1	D0521-2	D0521-3	PM003-60	PM003-71	19XS02-1	19XS02-2	19XS02-3	D0029-1	D0029-2	D0628-1	D0628-2	D3037-1	D3037-2	D3037-3
Gd	10.1	11.7	10.6	10.6	6.70	6.22	6.51	6.36	5.95	5.22	7.74	5.05	4.08	2.70	6.46	6.48	4.79	5.05	4.46
Tb	1.59	1.67	1.65	1.65	1.03	0.99	1.02	0.97	0.86	0.84	1.29	0.85	0.69	0.49	1.19	1.30	0.92	0.94	0.95
Dy	8.96	8.96	9.09	9.03	6.22	5.76	6.08	5.68	5.10	4.38	6.95	4.62	4.70	3.28	7.28	7.50	6.01	5.94	6.26
Ho	1.64	1.55	1.62	1.68	1.19	1.05	1.14	1.08	0.95	0.76	1.18	0.79	1.00	0.71	1.63	1.64	1.28	1.30	1.30
Er	4.40	4.10	4.29	4.33	3.08	2.90	3.00	2.90	2.58	1.91	3.11	2.05	2.87	2.10	4.62	4.69	3.97	3.90	3.82
Tm	0.61	0.54	0.60	0.61	0.42	0.41	0.41	0.41	0.39	0.26	0.39	0.26	0.42	0.31	0.67	0.70	0.62	0.59	0.62
Yb	3.59	3.34	3.68	3.62	2.73	2.49	2.65	2.54	2.28	1.44	2.39	1.54	2.75	2.00	4.36	4.52	4.13	3.88	3.62
Lu	0.53	0.47	0.54	0.54	0.37	0.35	0.37	0.36	0.33	0.22	0.35	0.22	0.40	0.30	0.65	0.68	0.64	0.58	0.56
Hf	5.12	4.83	5.32	5.06	4.63	4.14	4.40	4.22	3.70	4.37	6.48	4.08	2.43	1.35	3.48	3.43	3.32	3.61	3.30
Ta	2.19	2.44	2.33	2.25	1.46	1.31	1.44	1.35	1.11	1.49	2.80	1.35	0.14	0.059	0.20	0.21	0.20	0.21	0.30
Tl	0.05	0.07	0.05	0.06	0.12	0.18	0.14	0.26	0.20	0.28	0.07	0.18	0.23	0.16	0.057	0.064	0.41	0.38	0.50
Pb	5.57	5.07	4.75	4.75	3.90	4.18	4.04	3.69	7.73	11.80	19.20	2.99	4.82	4.73	3.99	8.74	10.5	12.3	7.62
Th	4.61	7.24	5.16	5.00	3.61	3.15	3.27	3.24	2.58	2.78	4.24	2.36	0.20	0.093	0.30	0.28	0.28	0.25	0.35
U	2.29	3.61	2.75	2.72	0.82	0.76	0.82	1.19	0.80	0.62	1.00	0.80	0.14	0.036	0.26	0.13	0.64	0.46	0.66
ΣREE	213	287	229	228	157	138	144	137	122	138	196	118	43.3	26.2	70.5	71.3	59.3	58.7	66.2
LREE/HREE	5.8	7.9	6.1	6.1	6.2	5.8	5.8	5.8	5.6	8.2	7.4	6.7	1.6	1.2	1.6	1.6	1.7	1.6	2.1
δEu	1.10	1.10	1.10	1.08	0.98	0.99	0.98	0.99	1.00	1.19	1.06	1.07	1.07	1.38	0.93	0.92	0.88	0.95	1.13
La_N/Yb_N	6.11	9.59	6.37	6.43	6.57	6.20	6.07	6.29	6.05	12.6	10.9	9.70	0.76	0.45	0.77	0.73	0.78	0.79	1.17

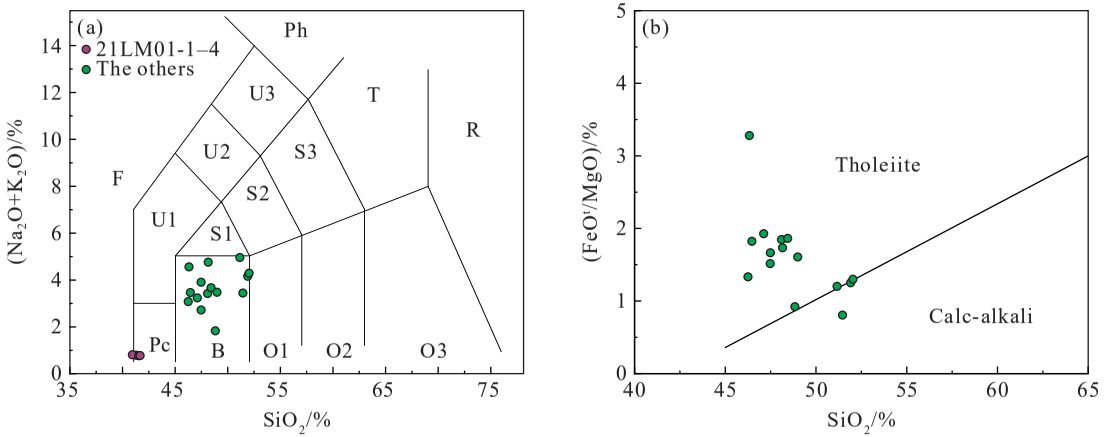

Fig. 5. a–SiO_2 *vs.* (K_2O+Na_2O) diagram (modified from Le Bas MJ et al., 1986); b–SiO_2 *vs.* (FeO^t/MgO) diagram (modified from Miyashiro A, 1974) of eclogite samples from the Jinshajiang orogenic belt. Pc–Picritic basalt; B–Basalt; O1–Basaltic andesite; O2–Andesite; O3–Dacite; R–Rhyolite; S1–Trachybasalt; S2–Basaltic trachyandesite; S3–Trachyandesite; T–Trachyte, trachydacite; F–Foidite; U1–Tephritebasanite; U2–Phonotephrite; U3–Tephriphonolite; Ph–Phonolite.

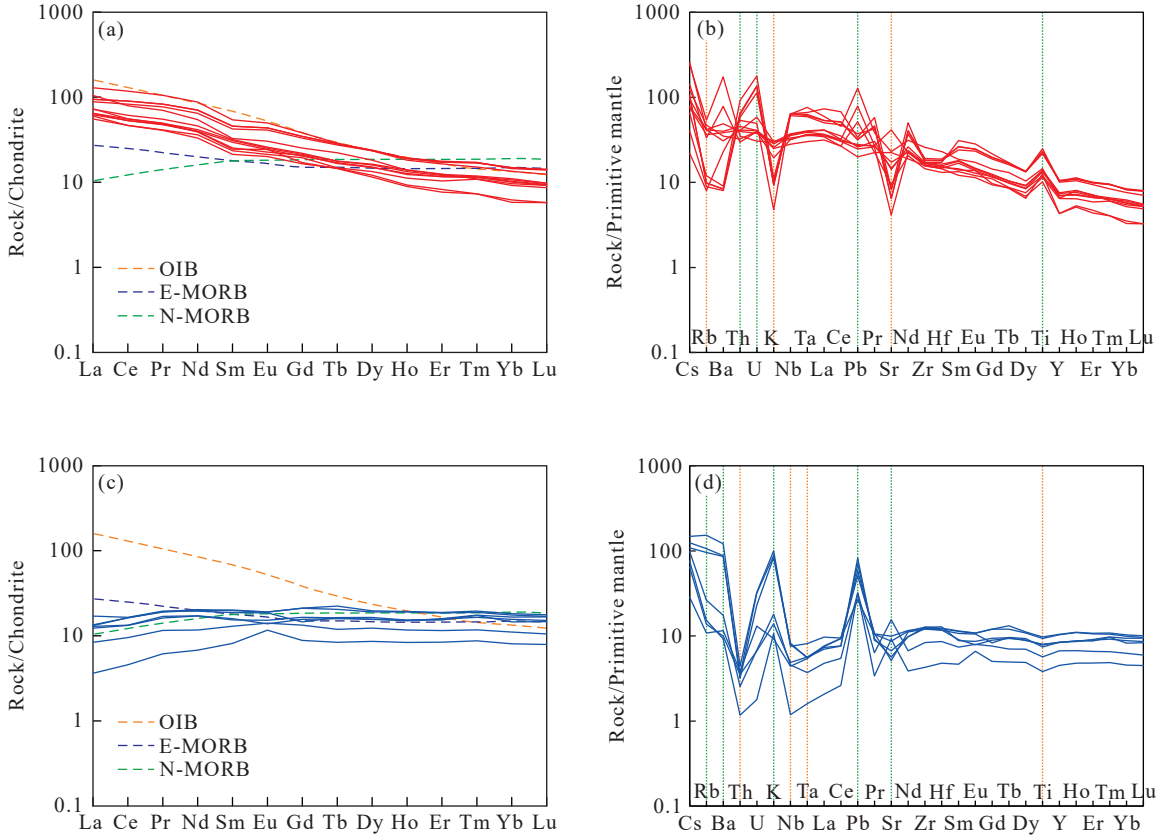

Fig. 6. a, c−The chondrite-normalized REE pattern diagram of samples; b, d− the primitive mantle-normalized trace-element spider diagram of samples (values of chondrites and primitive mantle from McDonough W and Sun SS, 1995).

show two different types of characteristics. Some samples are depleted in large ion lithophile elements (LILEs) such as Rb and K, relatively enriched with Pb and high field strength elements (HFSEs) such as Th, U and Ti (Fig. 6b). The other samples are obviously enriched with large ion lithophile elements (LILEs) such as Cs, Rb, Ba, K and Pb, and depleted with high field strength elements (HFSEs) such as Th, Nb, Ta and Ti (Fig. 6d). In the two group of samples, the variation of Sr element is irregular, which may be related to the later alteration of rocks.

4. Ar-Ar dating of retrograded eclogite and its hosting rock

4.1. Methods and process of Ar-Ar dating

The mineral separates (biotite and muscovite) were selected at the lab of Hebei Institute of Regional Geological and Mineral Resource Survey and the $^{40}Ar/^{39}Ar$ dating was carried out at the isotope thermochronological lab of the Institute of Geology, Chinese Academy of Geological Sciences. After ultrasonic cleaning, the cleaned pure mineral samples (purity > 99%) were encapsulated in quartz vials. This package was then placed into a nuclear reactor and irradiated with neutrons. The samples were irradiated in the Swimming Pool Reactor at the Institute of Atomic Energy, Chinese Academy of Sciences. Using channel B4, the reactor delivered a neutron flux of about 2.65×10^{13} $cm^{-2}s^{-1}$. The total irradiation time was 1440 mins and integral neutron flux was 2.29×10^{18} $cm^{-2}s^{-1}$. Meanwhile, a biotite reference sample ZBH-25 (132.7±1.2 Ma, and 7.6% K) was irradiated with neutrons together as a control sample.

A graphite furnace was used for step-heating of the samples, during which the samples were heated for 10 mins and purified for 20 min for each temperature increment. Mass spectrometry was carried out using a multicollector noble gas mass spectrometer Helix MC, with 20 sets of data collected for each peak value. Mass discrimination correction, atmospheric argon correction, blank correction, and interfering isotope correction were conducted for all data after they were regressed to the time zero values. The interfering isotope correction factors produced in the process of neutron irradiation were obtained by analyzing the irradiated K_2SO_4 and CaF_2 and they are $(^{36}Ar/^{37}Ar_o)_{Ca}$=0.0002398, $(^{40}Ar/^{39}Ar)_K$= 0.004782, and $(^{39}Ar/^{37}Ar_o)_{Ca}$=0.000806. Radioactive decay correction was carried out for ^{37}Ar, and the ^{40}K decay constant λ is 5.543×10^{-10} $year^{-1}$ (Steiger RH et al., 1977). The plateau ages, isochrone ages, and inverse isochrone ages were calculated with the program Ar-Ar CALC (Anthony Koppers, v2.5.2, 2012), with errors within 2σ. Detailed experimental processes are stated in relevant articles (Chen W et al, 2006; Zhang Y et al, 2006; Tang Y, 2020b).

4.2. Results of Ar-Ar dating

To constrain the metamorphism age of the (retrograded)

eclogites and to better understand their tectonic evolution, mineral separates (muscovite and biotite) from three samples taken from the Jinshajiang orogenic belt were selected for geochronological analyses. Sample PM003-71 is a garnet-albite-epidote-biotite actinolite schist chosen from the outcrop near Luomai Village (PM003, shown in Fig. 2). Samples D0521-1 and D0521-4 were taken from the same outcrop near the Congchang Village (D0521, shown in Figs. 2, 3). The former is an eclogite and the latter is the hosting rock (see Section 2 for detailed mineralogical characteristics). The detailed Ar-Ar dating results of micas through step-heating experiments are shown in Table 3.

As for the samples PM003-71 and D0521-1, muscovite separates were selected for $^{40}Ar/^{39}Ar$ dating. The total gas age of sample PM003-71 is 246 Ma, and nine steps from 820°C to 1180°C comprise a well-defined age plateau (Fig. 7a). Its plateau age is 247±2 Ma (MSWD=3.0), corresponding to 97.1% of ^{39}Ar release. According to the data of sample D0521-1, eleven steps from 780°C to 1400°C can be applied to age calculation, which yield a plateau age of of 248±2 Ma (MSWD=2.3) corresponding to 98.8% of ^{39}Ar release (Fig. 7c). The $^{40}Ar/^{36}Ar$-$^{39}Ar/^{36}Ar$ normal isochrone ages of these two samples are 247±2 Ma and 248±2 Ma (Figs. 7b, d), respectively. These initial $^{40}Ar/^{36}Ar$ are 291.2±11.8 (MSWD= 2.9) and 292.0±14.9 (MSWD=2.2), comparable to Nier value, indicating that there is no excess argon. According to microscopic observation, the muscovites feature narrow foliaceous occurrence, some of them exist in garnet center, and some are distributed between garnets and omphacites (Figs. 4a, b). Besides, the EPMA data and the calculation based on 22 oxygen atoms reveal that there are 6.43–6.77 Si cations in the muscovite, indicating that the muscovite is phengite and formed in the same metamorphic process as garnet and omphacite (Tang Y et al., 2020a). Therefore, the muscovite should be the product of eclogite facies metamorphism, and its Ar-Ar dating can reflect the metamorphism process that the samples experienced.

Muscovite and biotite separates from sample D0521-4 were selected for $^{40}Ar/^{39}Ar$ step-heating dating. According to the data, only six steps from 1020°C to 1400°C of biotite can be applied to age calculation, which yield a plateau age of 225±2 Ma (MSWD=11.0), whereas muscovite provides an older plateau age of 238±2 Ma (MSWD=1.3) calculation by twelve steps from 760°C to 1400°C (Figs. 7e, g). The $^{40}Ar/^{36}Ar$-$^{39}Ar/^{36}Ar$ normal isochrone ages of muscovite and biotite separates from the sample are 238±2 Ma and 224±3 Ma (Figs. 7f, h), respectively. These initial $^{40}Ar/^{36}Ar$ are 297.2±3.0 (MSWD=1.4) and 298.8±58.8 (MSWD=14.9), comparable to Nier value, indicating that there is no excess argon. In addition, the closure temperatures for muscovite and biotite in Ar-Ar (K-Ar) isotopic system are 450±50°C and 320±40°C, respectively (Harrison TM et al., 1985; Hames WE and Bowring SA, 1994; Tang Y et al., 2021, 2022b). Thus, the Ar-Ar ages can reflect the uplift process of eclogite and its hosting rocks, that is, the uplift to the shallow crust during 238−224 Ma.

5. Discussion

5.1. Protoliths of retrograded eclogites

The eclogites in Jinshajiang orogenic belt have undergone varying degrees of carbonate alteration and metamorphism, resulting in variable values of LOI and changes in the concentrations of mobile elements (e.g., Na, K, Ca, Cs, Rb, Ba, and Sr) compared with protolith values. However, the immobile elements (REE, Nb, Ta, Zr, Hf, Ti and P) and transition metal elements (V, Ni, Cr and Fe) are commonly thought to be least soluble when the precursor rocks are transformed to eclogites in the subduction zone and are therefore useful for determining provenance characteristics (Becker H et al., 2000; Chalot-Prat F et al., 2003; Spandler C et al., 2004; Bebout GE, 2007; Liu YS et al., 2008; Zhang RY et al., 2013; Wang HN et al., 2018). In this paper, four discrimination diagrams (Fig. 8) are used to decipher the petrogenesis and initial tectonic setting of eclogites.

Similar to the characteristics of Chondrite-normalized REE patterns and Primitive-mantle normalized trace element, the samples of eclogites ploted in discrimination diagrams can also be divided into two groups. In the Zr *vs.* TiO_2 diagram (Fig. 8a; Pearce JA, 1982), one group of the eclogites (Samples D0029, D0628 and D3037) fall in the field of MORB, and the other group plot in the field of within-plate basalts (WPB). In the Nb/Yb *vs.* Th/Yb diagram (Fig. 8b), all of the eclogites plot near the MORB–OIB array of Pearce JA (2008), with one group (Samples D0029, D0628 and D3037) very close to N-MORB field and the other group near the OIB field. Furthermore, one group fall into the N-MORB field (Fig. 8c) and D field (Fig. 8d) in the discrimination diagrams of Hf/3-Th-Ta (Wood DA, 1980) and Nb-Zr/4-Y (Meschede M, 1986), respectively. However, the other group plot in the boundary of E-MORB+WPT/WPAB (Fig. 8c) and A1+A2 (Fig. 8d) in the above ternary diagrams, respectively.

As discussed above, the protoliths of eclogites in the Jinshajiang orogenic belt are mainly divided into two types, one with oceanic island basalt (OIB) characteristics, and the other with N-MORB characteristics. Thus, it is concluded that the eclogites were mainly formed by subduction of the oceanic crust materials (oceanic island basalts and mid ocean ridge basalts) of the Jinshajiang Paleo-Tethys ocean.

5.2. Tectonic significance

Since the 1970s, predecessors have carried out a lot of research on passive continental margin of Jinshajiang orogenic belt, ophiolite, radiolarian siliceous rock of ocean basin, island arc magmatic rock, formation age of orogenic molasse and paleontological fossils, etc. (Zhong DL, 1998; Wang LQ et al., 1999; Wang XF et al., 2000; Pan GT et al., 2003; Sun XM and Jian P, 2004; Jian P et al., 2008, 2009; Fan WM et al., 2009; Zhu JJ et al., 2011; Dilek Y and Furnes H, 2011, 2014; Yin FG et al., 2021). Based on the previous understanding and the research data in this paper, the authors provided restrictions on the Paleo-Tethyan evolution process

Table 3. $^{40}Ar/^{39}Ar$ isotopic analytical data for step-heating experiments on mineral separates from eclogites.

T(°C)	$(^{40}Ar/^{39}Ar)_m$	$(^{36}Ar/^{39}Ar)_m$	$(^{37}Ar/^{39}Ar)_m$	$(^{38}Ar/^{39}Ar)_m$	^{40}Ar(%)	*F*	$^{39}Ar(\times10^{-14}mol)$	Age(Ma)	$\pm2\sigma$(Ma)
PM003-71 muscovite, Weight =13.71 mg, J=0.00395969 , TGA=246 Ma, WMA=247±2 Ma									
680	145.3664	0.3880	0.1065	0.0894	21.13	30.7180	4.1	207	13
760	63.7403	0.0940	0.0216	0.0305	56.41	35.9551	17.8	240	3
820	45.6179	0.0299	0	0.0176	80.65	36.7931	53.6	245	1
860	37.9219	0.0031	0.0030	0.0128	97.58	37.0024	95.2	247	1
900	37.2833	0.0011	0	0.0126	99.10	36.9462	317	246	1
940	38.0366	0.0038	0	0.0134	97.08	36.9242	49.8	246	1
980	37.5201	0.0021	0.0003	0.0128	98.33	36.8920	91.0	246	1
1020	37.6561	0.0016	0	0.0127	98.76	37.1900	106	248	1
1060	39.5717	0.0080	0.0082	0.0148	94.01	37.2001	15.9	248	2
1120	42.1271	0.0168	0	0.0151	88.20	37.1556	7.4	248	4
1180	42.6743	0.0171	0	0.0148	88.18	37.6318	7.9	251	4
1400	67.6497	0.1211	0	0.0451	47.10	31.8618	0.6	214	45
D0521-1 muscovite, Weight =13.6 mg, J=0.00400121, TGA=247 Ma, WMA=248±2 Ma									
650	157.7601	0.4494	0	0.0994	15.82	24.9553	4.3	172	13
720	148.4364	0.3959	0.1215	0.0884	21.18	31.4469	9.3	214	10
780	41.1527	0.0155	0.0115	0.0155	88.88	36.5758	38.2	246	1
820	39.9683	0.0108	0	0.0144	92.02	36.7803	44.9	248	1
860	39.6806	0.0094	0.0013	0.0140	92.98	36.8970	81.6	248	1
900	39.6278	0.0094	0.0009	0.0143	92.96	36.8378	117	248	1
940	37.7039	0.0029	0.0061	0.0130	97.71	36.8400	296	248	1
980	37.6422	0.0031	0.0016	0.0129	97.55	36.7206	307	247	1
1020	38.4000	0.0055	0.0027	0.0134	95.77	36.7754	148	248	1
1070	38.1167	0.0046	0.0047	0.0136	96.45	36.7625	55.3	248	1
1120	38.4528	0.0055	0	0.0132	95.76	36.8236	35.2	248	1
1200	39.3426	0.0073	0	0.0140	94.54	37.1947	21.5	250	2
1400	43.0986	0.0217	0.0354	0.0161	85.09	36.6747	13.8	247	2
D0521-4 muscovite, Weight =13.18mg, J=0.00400856, TGA=237 Ma, WMA=238±2 Ma									
650	290.6280	0.9067	0	0.1828	7.81	22.7089	6.1	157	23
700	135.4288	0.3449	0.0020	0.0784	24.75	33.5176	13.4	227	9
760	87.1492	0.1754	0.0076	0.0457	40.51	35.3053	43.1	239	4
800	91.2200	0.1897	0	0.0477	38.54	35.1587	53.4	238	5
840	50.0122	0.0499	0.0070	0.0219	70.53	35.2714	117	239	1
880	38.4813	0.0110	0	0.0144	91.53	35.2231	185	238	1
920	36.5986	0.0049	0.0026	0.0134	96.01	35.1371	170	238	1
960	36.6134	0.0052	0.0038	0.0134	95.82	35.0828	136	237	1
1000	37.9184	0.0095	0	0.0142	92.57	35.1025	91.3	238	1
1040	38.9075	0.0124	0	0.0146	90.58	35.2407	42.5	238	1
1100	38.4652	0.0114	0.0221	0.0146	91.23	35.0920	72.4	237	1
1150	38.6531	0.0135	0.0809	0.0180	89.68	34.6663	10.1	235	5
1250	39.3174	0.0138	0.0164	0.0148	89.64	35.2431	31.2	238	1
1400	39.3041	0.0134	0	0.0147	89.94	35.3502	35.7	239	1
D0521-2 biotite, Weight =13.18 mg, J=0.00398519, TGA=215 Ma, WMA=225±2 Ma									
650	105.9797	0.3375	0.0025	0.0812	5.91	6.2611	12.3	44.5	9
710	50.0550	0.0951	0.0099	0.0357	43.84	21.9461	46.6	151	3
760	40.7520	0.0313	0	0.0230	77.33	31.5124	89.8	213	1
800	36.1781	0.0144	0.0080	0.0193	88.26	31.9303	86.5	216	1
840	34.2544	0.0070	0.0026	0.0176	93.95	32.1816	100	218	1
880	33.9774	0.0066	0.0269	0.0176	94.30	32.0424	70.4	217	1
920	34.6077	0.0068	0	0.0174	94.19	32.5984	20.8	220	1
960	34.2368	0.0057	0.0247	0.0176	95.12	32.5679	16.5	220	2
1020	34.5906	0.0032	0.0006	0.0173	97.22	33.6296	137	227	1
1060	33.9721	0.0025	0	0.0168	97.86	33.2454	171	224	1
1120	34.0092	0.0032	0.0028	0.0166	97.22	33.0641	64.8	223	1
1160	33.9748	0.0028	0	0.0161	97.55	33.1430	59.1	224	1
1200	37.7806	0.0141	0	0.0175	88.94	33.6018	10.0	227	3
1400	50.5055	0.0614	0	0.0248	64.08	32.3663	5.3	219	6

Notes: F is the ratio of radiogenic Argon 40 and Argon 39.

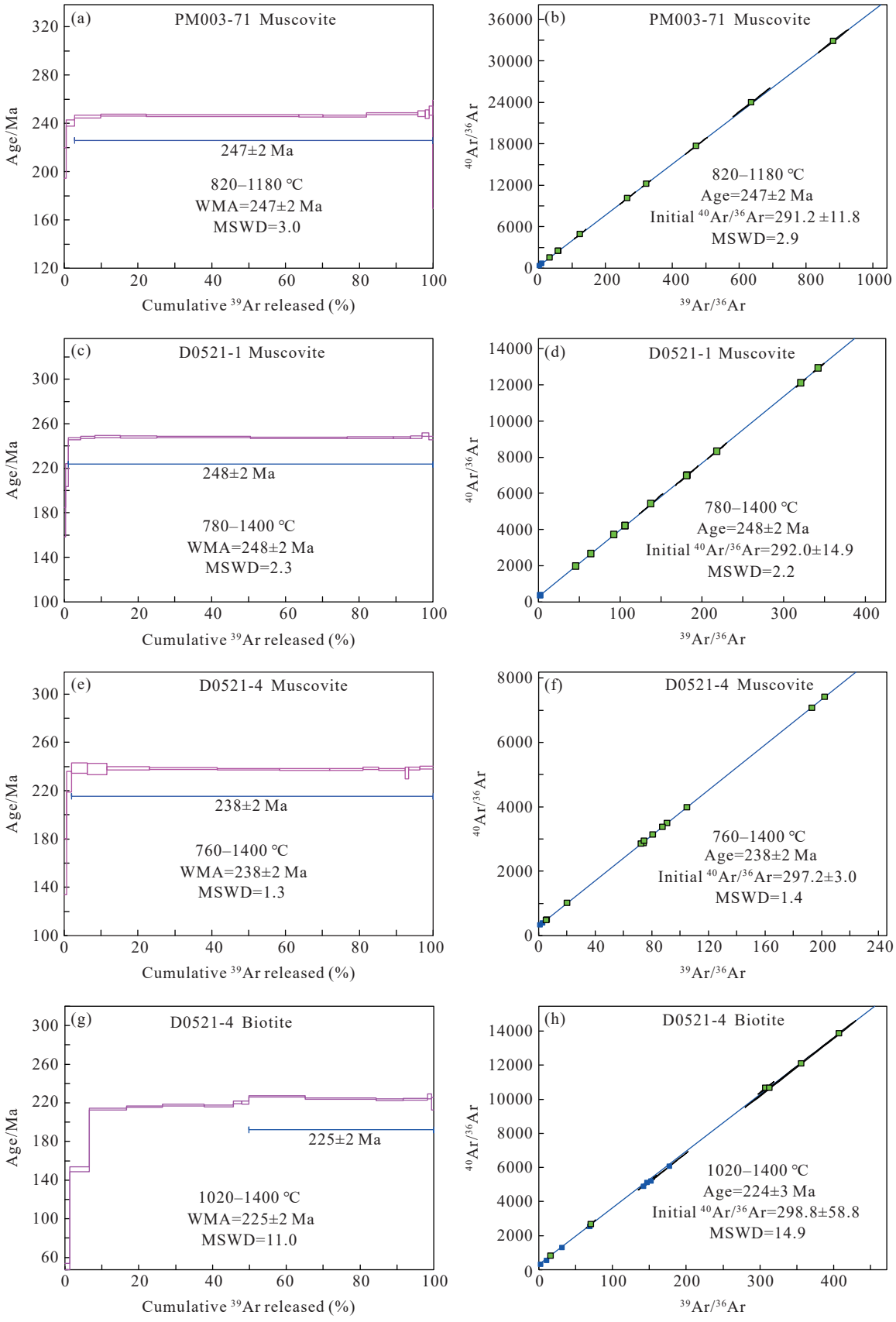

Fig. 7. ^{40}Ar/^{39}Ar plateau age and ^{40}Ar/^{36}Ar-^{39}Ar/^{36}Ar isochron age of biotite and muscovite from samples. WMA –weighted mean age; MSWD–mean square of weighted deviates.

in Jinshajiang orogenic belt and divided it into five major evolution stages (Fig. 9), that is, the stages of rift basin (D), oceanic basin spreading (C_1–P_1), oceanic crust subduction (P_1^2–P_3), early stage of arc-continent collision (T_1–T_2^1) and

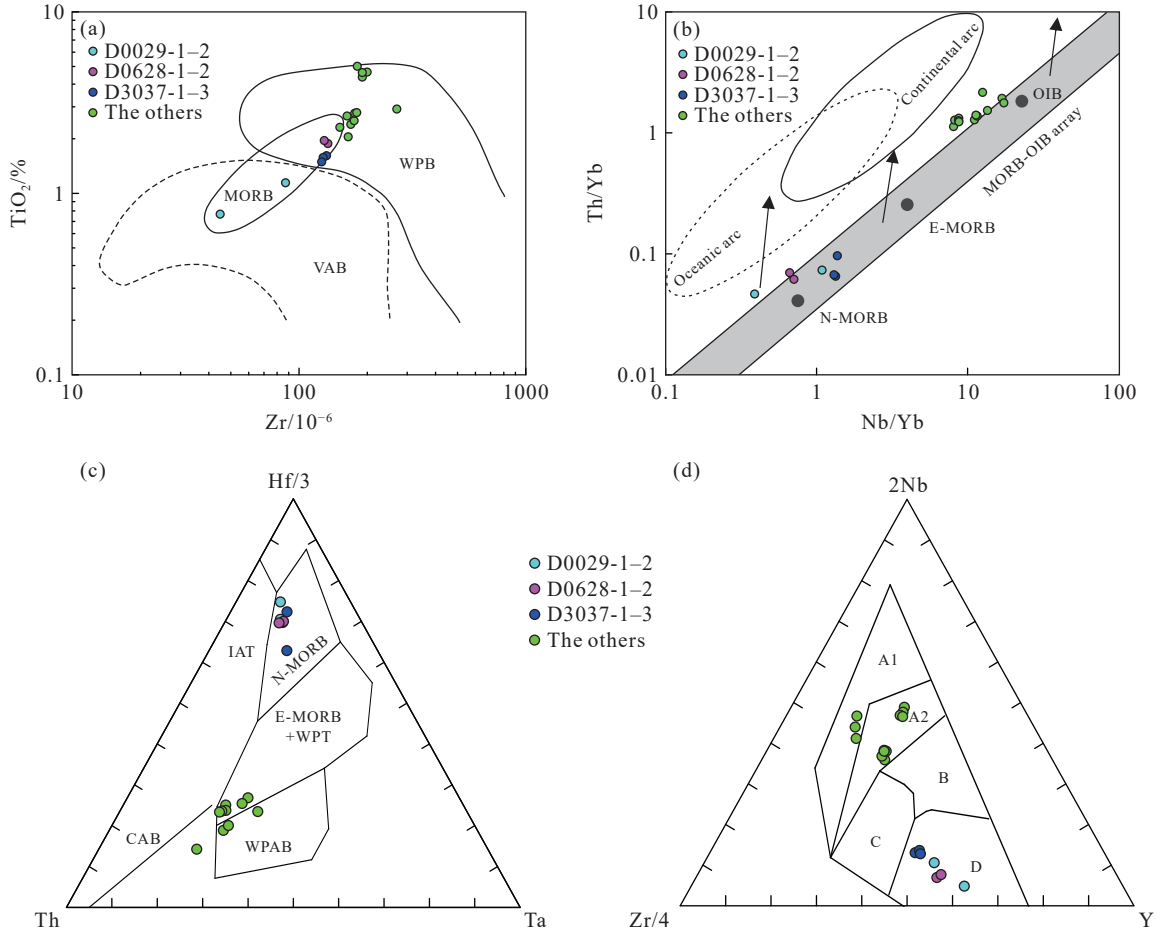

Fig. 8. Discrimination diagrams for the eclogites. a−Zr *vs.* TiO_2 (Pearce JA, 1982); b−Nb/Yb *vs.* Th/Yb (Pearce JA, 2008); c−Hf/3-Th-Ta (Wood DA, 1980); d−2Nb-Zr/4-Y (Meschede M, 1986). MORB−mid ocean ridge basalt; WPB−within-plate basalts; VAB−volcanic arc basalt; OIB−oceanic island basalt; E-MORB−enriched MORB; N-MORB−normal MORB; WPAB−within plate alkaline basalt; WPT−within plate tholeiite; IAT−island arc tholeiite; CAB−calc-alkaline basalt; A1−intraplate alkali basalt; A2−intraplate alkali basalt and tholeiite; B−E-MORB; C−intraplate tholeiite and volcanic arc basalt; D−N-MORB and volcanic arc basalt.

large-scale collision-orogeney (T_3^1–T_3^2). Later, the Jinshajiang orogenic belt underwent a post collision extension and foreland basin development (T_3^2–K) and subsequent intracontinental convergence (E–Q).

The Jinshajiang Paleo-Tethys ocean basin began to subduct westward in the Middle Permian (P_1^2). On the west side of the Jinshajiang ocean basin, the oceanic crust subducted under the Qamdo-Lanping continental crust. The Deqin-Weixi Permian continental marginal arc and the Qamdo-Lanping back arc basin (continental crust basement) on the west side were formed respectively during the Middle to Late Permian (P_2–P_3) (Wang BD et al., 2014, 2018, 2021). The continental clastic rocks and a large number of intermediate acid volcanic rocks of Malasongduo Formation (248–244 Ma) are in unconformable contacts with the underlying strata, marking the beginning of arc-continent collision (T_1–T_2^1) (Zi JW et al., 2012a, 2012b, 2013; Wang LQ et al., 2013; Yu YS et al., 2019, Wu Z et al., 2021). The newly discovered eclogites in the Gonjo area, are products of the closure of the lithosphere of the Jinshajiang Paleo-Tethys ocean and collision between the Qamdo block and Zhongza continental block, which can provide more direct evidence for precisely defining the timing of the closure of Jinshajiang Paleo-Tethys ocean and subsequent arc-continent collision process (Tang Y et al., 2020a, 2022a).

Combined with the characteristics of major and trace elements in the whole rock of the samples, the Jinshajiang eclogites were formed due to the subduction of oceanic crust materials (OIB or/and N-MORB). According to the data of electron probe micro analysis of eclogite (Tang Y et al., 2020a), the temperature and pressure of eclogite facies metamorphism were P≈2.2–2.34 GPa and T≈622–688°C respectively as measured with geobarometry Grt-Omp-Phe and geothermometer Grt-Omp, indicating that the subduction depth of oceanic crust materials was at least 70 km. The Ar-Ar plateau ages of muscovite (phengite) from two eclogite samples obtained in this paper are 247±2 Ma and 248±2 Ma respectively. In addition, the zircon U-Pb ages of eclogite samples obtained from previous studies are ~244Ma, and the zircons of eclogite samples have very low Th/U ratio (<0.01), Nb, Ta and HREE contents without negative Eu anomaly (Tang Y et al., 2020a). Thus, the zircon U-Pb ages should be metamorphic zircons of eclogite facies. It can be concluded that the peak metamorphic age of eclogite facies was about 248–244 Ma, representing the timing of complete closure of the Jinshajiang Paleo-Tethys ocean. It further shows that arc-

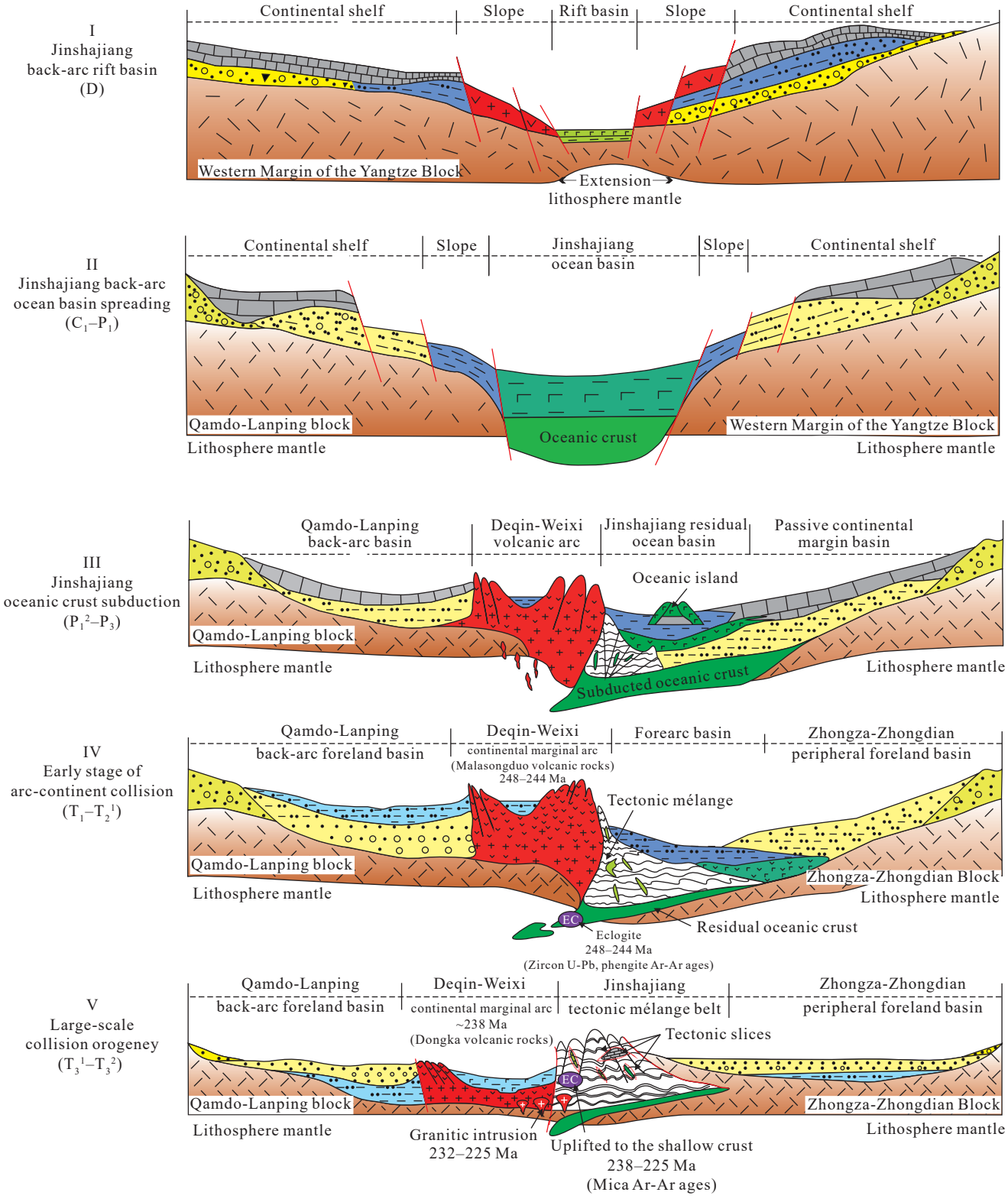

Fig. 9. Schematic diagram of tectonic evolution of Jinshajiang Paleo-Tethys orogenic belt (modified from Wang LQ et al., 1999) .

continent collision between Deqin-Weixi continental margin arc and Zhongza continental block had been initiated since 248–244 Ma (T_2^1).

Later, the eclogites were detached from the subduction plate and quickly exhumed to the shallow crust. In this paper, muscovite and biotite are selected from the hosting rocks of eclogite for Ar-Ar isotopic dating. The Ar-Ar plateau ages obtained are 238±2 Ma and 225±2 Ma respectively, reflecting the exhumation age of eclogites and their hosting rocks during 238–225 Ma, which can be interpreted as the timing of large-scale arc (continent)-continent collision between the Deqin-Weixi continental margin arc and Zhongza block (T_3^1–T_3^2). During this process, the intermediate-basic metamorphic igneous rocks in the thickened lower crust partially melted,

and then formed large-scale granitic intrusive rocks. Previous studies have shown that the granites in this period have the characteristics of syn-collisional granite (232–225 Ma, Gong XD et al., 2020). Since then, the region had entered a post collision extension period. The development of purple-red conglomerate and sandstone (Upper Triassic Jiapila Formation) in the region, which have the characteristics of molasse formation, marks the end of the evolution of the Jinshajiang Paleo-Tethys in eastern Tibet (Wang BD et al., 2014, 2018, 2021; Tang Y et al., 2022a).

6. Conclusion

(i) The analysis data of major and trace elements of the whole rock of eclogite samples reveal that the protoliths of eclogites are mainly divided into two types, one with the characteristics of oceanic island basalt (OIB) and the other with the characteristics of normal mid ocean ridge basalt (N-MORB). It shows that the eclogites in Gonjo area were formed by the deep subduction of the oceanic crust materials in the Jinshajiang Paleo-Tethys ocean.

(ii) The Ar-Ar plateau ages of muscovite (phengite) from two eclogite samples are 247±2 Ma and 248±2 Ma respectively. Combined with zircon U-Pb ages (~244Ma) and trace element characteristics of eclogite samples, it is believed that the peak metamorphic age of eclogite facies was about 248–244 Ma, and the Jinshajiang Paleo-Tethys ocean had been completely closed since 248–244 Ma (T_2^1).

(iii) The Ar-Ar plateau ages of muscovite and biotite selected from the hosting rocks of eclogite are 238±2 Ma and 225±2 Ma respectively, reflecting the exhumation age of eclogites and their hosting rocks during 238–225 Ma. It can be interpreted as the timing of large-scale arc (continent)-continent collision between the Deqin-Weixi continental margin arc and Zhongza block (T_3^1–T_3^2).

CRediT authorship contribution statement

Yuan Tang and Dong-bing Wang conceived of the presented idea. Yuan Tang and Xiao-dong Gong carried out the experiments. Ya-dong Qin and Yong Li contributed to sample collection. Yuan Tang and Xiao-dong Gong contributed to the figures. Yuan Tang, Dong-bing Wang and Bao-di Wang contributed to the interpretation of the results. Yuan Tang took the lead in writing the manuscript. All authors provided critical feedback and helped shape the research, analysis and manuscript.

Declaration of competing interest

The authors declare no conflicts of interest.

Acknowledgment

This research was jointly funded by two Second Tibetan Plateau Comprehensive Scientific Investigation and Research Projects (2019QZKK0702, 2019QZKK0706), a project of National Natural Science Foundation of China (42230311) and two geological survey projects of China Geological Survey (DD20221635, DD20221811).

References

Bebout GE. 2007. Metamorphic chemical geodynamics of subduction zones. Earth and Planetary Science Letters, 260(3), 373–393. doi: 10.1016/j.epsl.2007.05.050.

Becker H, Jochum KP, Carlson RW. 2000. Trace elements fractionation during dehydration of eclogite from high-pressure terranes and the implications for element fluxes in subduction zones. Chemical Geology, 163, 65–69. doi: 10.1016/s0009-2541(99)00071-6.

Carswell DA, Harley SI. 1990. Mineral barometry and thermometry. In:Carswell DA (ed.). Eclogite Facies Rocks. Blackie, Glasgow, 83–110.

Chalot-Prat F, Ganne J, Lombard A. 2003. No significant element transfer from the oceanic plate to the mantle wedge during subduction and exhumation of the Tethys lithosphere (Western Alps). Lithos, 69, 69–103. doi: 10.1016/s0024-4937(03)00047-1.

Chen W, Zhang Y, Zhang YQ, Jin GS, Wang QL. 2006. Late Cenozoic episodic uplifting in southeastern part of the Tibetan plateau-evidence from Ar-Ar thermochronology. Acta Petrologica Sinica, 22(4), 867–872 (in Chinese with English abstract). doi: 10.1016/j.sedgeo.2005.11.021.

Dilek Y, Furnes H. 2011. Ophiolite genesis and global tectonics: geochemical and tectonic fingerprinting of ancient oceanic lithosphere. Geological Society of America Bulletin, 123, 387–411. doi: 10.1130/b30446.1.

Dilek Y, Furnes H. 2014. Ophiolites and their origins. Elements, 10, 93–100. doi: 10.2113/gselements.10.2.93.

Fan WM, Peng TP, Wang YJ. 2009. Triassic magmatism in the southern Lancangjiang zone, southwestern China and its constraints on the tectonic evolution of Paleo-Tethys. Earth Science Frontiers, 16(6), 291–302 (in Chinese with English abstract). doi: 10.3321/j.issn:1005-2321.2009.06.031.

Gong XD, Tang Y, Qin YD, Wang BD, Wang DB, Liu H, Duan YY. 2020. Late Triassic collision of Jinshajiang suture belt: Geochronological, geochemical and Hf Isotope evidences from Quartz Monzonite in Gonjo area. Earth Science, 45(8), 2905–2919 (in Chinese with English abstract). doi: 10.3799/dqkx.2020.221.

Guan C, Yan MD, Zhang WL, Zhang DW, Fu Q, Yu L, Xu WL, Zan JB, Li BS, Zhang T, Shen M. 2021. Paleomagnetic and chronologic data bearing on the Permian/Triassic boundary position of Qamdo in the eastern Qiantang terrane: Implications for the closure of the Paleo Tethys. Geophysical Research Letters, 48(6), 1–10. doi: 10.1029/2020GL092059.

Hames WE, Bowring SA. 1994. An empirical evaluation of the argon diffusion geometry in muscovite. Earth and Planetary Science Letters, 124, 161–167. doi: 10.1016/0012-821x(94)00079-4.

Harrison TM, Duncan I, Mcdougall I. 1985. Diffusion of ^{40}Ar in biotite: temperature, pressure and compositional effects. Geochimica et Cosmochimica Acta, 49, 2461–2468. doi: 10.1016/0016-7037(85)90246-7.

Huang K, Opdyke ND. 2016. Paleomagnetism of the Upper Triassic rocks from south of the Ailaoshan Suture and the timing of the amalgamation between the South China and the Indochina Blocks. Journal of Asian Earth Sciences, 119, 118–127. doi: 10.1016/j.jseaes.2015.12.005.

Jian P, Liu D, Kroner A, Zhang Q, Wang YZ, Sun XM, Zhang W. 2009. Devonian to Permian plate tectonic cycle of the Paleo-Tethys Orogen in southwest China (II): insights from zircon ages of ophiolites, arc/back-arc assemblages and within-plate igneous rocks and

generation of the Emeishan CFB province. Lithos, 113, 767–784. doi: 10.1016/j.lithos.2009.04.006.

Jian P, Liu DY, Sun XM. 2008. SHRIMP dating of the Permo-Carboniferous Jinshajiang ophiolite, southwestern China: Geochronological constraints for the evolution of Paleo-Tethys. Journal of Asian Earth Sciences, 32, 371–384. doi: 10.1016/j.jseaes.2007.11.006.

Le Bas MJ, Le Maitre RW, Streckeisen A, Zanenin B. 1986. A chemical classification of volcanic rocks based on the total alkali - silica diagram. Journal of Petrology, 27(3), 745–750. doi: 10.1093/petrology/27.3.745.

Li XZ, Liu WJ, Wang YZ, Zhu QW. 1999. The tectonic evolution and metallogenesis in the tehys of the Nujiang-Langcangjiang-Jinshajiang area, southwestern china. Beijing: Geological Publishing House, 45–73, 122–132 (in Chinese with English abstract).

Liu YS, Zong KQ, Kelemen PB, Gao S. 2008. Geochemistry and magmatic history of eclogites and ultramafic rocks from the Chinese continental scientific drill hole: subduction and ultrahigh-pressure metamorphism of lower crustal cumulates. Chemical Geology, 247, 133–153. doi: 10.1016/j.chemgeo.2007.10.016.

Liu ZQ, Li XZ, Ye QT, Luo JN, Shen GF, Yang YQ. 1993. Division of Tectono-Magmatic zones and the distribution of deposits in the Sanjiang area. Beijing: Geological Publishing House, 6 –89 (in Chinese with English abstract).

McDonough WF, Sun SS. 1995. The composition of the Earth. Chemical Geology, 120(3–4), 223–253. doi: 10.1016/0009-2541(94)00140-4.

Meschede M. 1986. A method of discriminating between different types of mid-ocean ridge basalts and continental tholeiites with the Nb–Zr–Y diagram. Chemical Geology, 56, 207–218. doi: 10.1016/0009-2541(86)90004-5.

Metcalfe I. 2006. Palaeozoic and Mesozoic tectonic evolution and palaeogeography of East Asian crustal fragments: the Korean Peninsula in context. Gondwana Research, 9, 24–46. doi: 10.1016/j.gr.2005.04.002.

Miyashiro A. 1974. Volcanic rock series in island arc and active continental margins. American Journal of Science, 274(4), 321–355. doi: 10.2475/ajs.274.4.321.

Pan GT, Xu Q, Hou ZQ, Wang LQ, Du DX, Mo XX, Li DM, Wang MJ, Li XZ, Jiang XS. 2003. Archipelagic orogenesis, metallogenic systems and assessment of the mineral resources along the Nujiang-Langcangjiang-Jinshajiang area in southwestern China. Beijing: Geological Publishing House, 11 –79 (in Chinese with English abstract).

Pearce JA. 1982. Trace elements characteristic of lavas from destructive plate boundaries. Andesites[C]//Thorpe R S. Orogenic andesites and related rocks. Chichester, England: John Wiley & Sons, 525–548.

Pearce JA. 2008. Geochemical fifingerprinting of oceanic basalts with applications to ophiolite classifification and the search for Archean oceanic crust. Lithos, 100, 14–48. doi: 10.1016/j.lithos.2007.06.016.

Song PP, Ding L, Li ZY, Lippert PC, Yang TS, Zhao XX, Fu JJ, Yue YH. 2015. Late Triassic paleolatitude of the Qiangtang block: Implications for the closure of the Paleo-Tethys Ocean. Earth and Planetary Science Letters, 424, 69–83. doi: 10.1016/j.epsl.2015.05.020.

Spandler C, Hermann J, Arculus R, Mavrogenes J. 2004. Geochemical heterogeneity and element mobility in deeply subducted oceanic crust: insights from high-pressure mafic rocks from New Caledonia. Chemical Geology, 206, 21–42. doi: 10.1016/j.chemgeo.2004.01.006.

Steiger RH, Jager E. 1977. Subcommission on geochronology: convention on the use of decay constants in geo- and cosmochronology. Earth and Planetary Science Letters, 36, 359–362. doi: 10.1016/0012-821X(77)90060-7.

Sun SS, McDonough WF. 1989. Chemical and isotopic systematics of oceanic basalts: Implications for mantle composition and processes. geological society, London, Special Publication, 42, 313 –345. doi: 10.1144/GSL.SP.1989.042.01.19.

Sun XM, Jian P. 2004. The Wilson cycle of the Jinshajiang paleo-Tethys Ocean, in western Yunnan and western Sichuan Province. Geological Review, 50, 343–350 (in Chinese with English abstract). doi: 10.16509/j.georeview.2004.04.002.

Tang Y, Liu YP, Wang P, Tang WQ, Qin YD, Gong XD, Wang DB, Wang BD. 2021. A new understanding of Demala Group complex in Chayu Area, southeastern Qinghai-Tibet Plateau: evidence from zircon U-Pb and mica $^{40}Ar/^{39}Ar$ dating. China Geology, 4, 77–94. doi: 10.31035/cg2021021.

Tang Y, Qin YD, Gong XD, Duan YY, Chen G, Yao HY, Liao JX, Liao SY, Wang DB, Wang BD. 2020a. Discovery of eclogites in Jinsha River suture zone, Gonjo County, eastern Tibet and its restriction on Paleo-Tethyan evolution. China Geology, 1, 83–103. doi: 10.31035/cg2020003.

Tang Y, Qin YD, Gong XD, Liu H, Wang DB, Wang BD. 2022a. Determination of material composition of Jinshajiang tectonic melange belt in Gonjo -Baiyu area, eastern Tibet. Sedimentary Geology and Tethyan Geology, 42(2), 260–278 (in Chinese with English abstract). doi: 10.19826/j.cnki.1009-3850.2022.04015.

Tang Y, Wang DB, Liao SY, Wang BD, Yin FG. 2020b. Fabrics and $^{40}Ar/^{39}Ar$ ages of metamorphic rocks in the Gaoligong tectonic belt: implications for Cenozoic metamorphism and deformation in the SE Tibetan Plateau. Journal of Asian Earth Sciences, 192. doi: 10.1016/j.jseaes.2020.104270.

Tang Y, Wang P, Deng H, Liu YP, Tang WQ. 2022b. Petrological records of major tectono-magmatic events since Oligocene in the southeastern segment of Xianshuihe fault zone in the eastern margin of Tibetan Plateau. Geological Bulletin of China, 41(7), 1121–1143 (in Chinese with English abstract). doi: 10.12097/j.issn.1671-2552.2022.07.001.

Wang BD, Wang LQ, Wang DB, Li FQ, Tang Y, Wang QY, Yan GC, Wu Z. 2021. The temporal and spatial framework and its tectonic evolution of the Jinsha River arc-basin system, Southwest China. Sedimentary Geology and Tethyan Geology, 41(2), 246–264 (in Chinese with English abstract). doi: 10.19826/j.cnki.1009-3850.2021.02008.

Wang BD, Wang LQ, Wang DB, Yin FG, He J, Peng ZM, Yan GC. 2018. Tectonic evolution of the Changning-Menglian Proto-Paleo Tethys Ocean in the Sanjiang Area, Southwestern China. Earth Science, 43(08), 2527–2550 (in Chinese with English abstract). doi: 10.3799/dqkx.2018.160.

Wang BD, Wang LQ, Chen JL, Yin FG, Wang DB, Zhang WP, Chen LK, Liu H. 2014. Triassic three-stage collision in the Paleo-Tethys: Constraints from magmatism in the Jiangda-Deqen-Weixi continental margin arc, SW China. Gondwana Research, 26(2), 475–491. doi: 10.1016/j.gr.2013.07.023.

Wang HN, Liu FL, Li J, Sun ZB, Ji L, Tian Z, Liu L, Santosh M. 2018. Petrology, geochemistry and *P-T-t* path of lawsonite-bearing retrograded eclogites in the Changning-Menglian orogenic belt, southeast Tibetan Plateau. Journal of Metamorphic Geology, 37(4), 439–478. doi: 10.1111/jmg.12462.

Wang LQ, Pan GT, Li DM, Xu Q, Lin SL. 1999. The spatio-temporal framework and geological evolution of the Jinshajiang Arc-Basin systems. Act Geological Sinica, 73, 206–218 (in Chinese with English abstract). doi: 10.19762/j.cnki.dizhixuebao.1999.03.002.

Wang XF, Metcalfe I, Jian P, He LQ, Wang CS. 2000. The Jinshajiang-Ailaoshan suture zone, China tectonostratigraphy, age and evolution. Journal of Asian Earth Sciences, 18, 675–690. doi: 10.1016/S1367-9120(00)00039-0.

Wood DA. 1980. The application of a Th-Hf-Ta diagram to problems of tectonomagmatic classification and to establishing the nature of crystal contamination of basaltic lavas of the British Tertiaty Volcanic Province. Earth and Planetary Science Letters, 50(1),

11–30. doi: 10.1016/0012-821x(80)90116-8.

Wu FY, Wan B, Zhao L, Xiao WJ, Zhu RX. 2020. Tethyan geodynamics. Acta Petrologica Sinica, 36(6), 1627–1674 (in Chinese with English abstract). doi: 10.18654/1000-0569/2020.06.01.

Wu Z, Ji JP, Wang BD, Tang Y, Qin YD, Gong XD, He J. 2021. Zircon U-Pb age, geochemical characteristics and constraints on the Jinshajiang Paleo-Tethys collision of Early-Middle Triassic Malasongduo Formation volcanic rocks from the Gongjue area, Eastern Tibet. Geological Bulletin of China, 40(11), 1877–1891 (in Chinese with English abstract). doi: 10.12097/j.issn.1671-2552.2021.11.007.

Xu ZQ, Dilek Y, Cao H, Yang JS, Robinson P, Ma CQ, Li HQ, Jolivet M, Roger F, Chen XJ. 2015. Paleo-Tethyan evolution of Tibet as recorded in the East Cimmerides and West Cathaysides. Journal of Asian Earth Sciences, 105, 320–337. doi: 10.1016/j.jseaes.2015.01.021.

Yan YG, Zhao Q, Zhang YP, Huang BC, Zheng WJ, Zhang PZ. 2019. Direct Paleomagnetic constraint on the closure of Paleo‐Tethys and its implications for linking the Tibetan and southeast Asian Blocks. Geophysical Research Letters, 46, 14368–14376. doi: 10.1029/2019GL085473.

Yang JS, Xu ZQ, Geng QR, Li ZL, Xu XZ, Li TF, Ren YF, Li HQ, Cai ZH, Liang FH, Chen SN. 2006. A possible new HP/UHP? metamorphic belt in China: Discovery of eclogite in the Lhasa terrane, Tibet Act Geological Sinica, 8(12), 1787–1792 (in Chinese with English abstract). doi: 10.1111/j.1745-4557.2006.00081.x.

Yang JS, Xu ZQ, Li TF, Li HQ, Li ZL, Ren YF, Xu XZ, Chen SY. 2007. Oceanic subduction-type eclogite in the Lhasa block, Tibet, China: Remains of the Paleo-Tethys ocean basin? Geological Bulletin of China, 26(10), 1277–1287. doi: 10.1016/S1872-5791(07)60044-X.

Yin FG, Xu B, Wang DB, Wang BD, Tang Y. 2021. Early Paleozoic magmatic event in the Sanjiang orogenic belt in southwest China and its response to the evolution of the Proto-Tethyan Ocean. Geological Bulletin of China, 40(6), 817–826 (in Chinese with English abstract). doi: 10.12097/j.issn.1671-2552.2021.06.001.

Yu YS, Zhang H, Wang FM, Wang XM, Liu BZ, Qin FY, He H. 2019. Age and geochemical characteristics of Malasongduo Formation rhyolite in Riza Mountain, east Tibet, and its geological significance. Geological Bulletin of China, 38(05), 697–710 (in Chinese with English abstract). doi: 10.12097/j.issn.1671-2552.2019.05.001.

Zhai QG, Zhang RY, Jahn BM, Li, C, Song SG, Wang J. 2011. Triassic eclogites from central Qiangtang, northern Tibet, China: petrology, geochronology and metamorphic *P-T* path. Lithos, 125, 173–189. doi: 10.1016/j.lithos.2011.02.004.

Zhang RY, Lo CH, Chung SL, Grove M, Omori S, Iizuka Y, Liou JG, Tran VT. 2013. Origin and tectonic implication of ophiolite and eclogite in the Song Ma Suture Zone between the South China and Indochina Blocks. Journal of Metamorphic Geology, 31, 49–62. doi: 10.1111/jmg.12012.

Zhang Y, Chen W, Chen KL, Liu XY. 2006. Study on the Ar-Ar age spectrum of diagenetic I/S and the mechanism of ^{39}Ar recoil loss-Examples from the clay minerals of P-T boundary in Changxing, Zhejiang Province. Geological Review, 52(4), 556–561 (in Chinese with English abstract). doi: 10.3321/j.issn:0371-5736.2006.04.015.

Zhong DL. 1998. The Paleotethys orogenic belt in west of Sichuan and Yunnan. Science Publishing House, Beijing, 1–230 (in Chinese with English abstract).

Zhu JJ, Hu RZ, Bi XW, Zhong H, Chen H. 2011. Zircon U-Pb ages, Hf-O isotopes and whole-rock Sr-Nd-Pb isotopic geochemistry of granitoids in the Jinshajiang suture zone, SW China: constraints on petrogenesis and tectonic evolution of the Paleo-Tethys Ocean. Lithos, 126, 248–264. doi: 10.1016/j.lithos.2011.07.003.

Zi JW, Cawood PA, Fan WM, Tohver E, Wang YJ, McCuaig TC, Peng TP. 2013. Late Permian-Triassic magmatic evolution in the Jinshajiang orogenic belt, SW China and implications for orogenic processes following closure of the Paleo-Tethys. American Journal of Science, 313, 81–112. doi: 10.2475/02.2013.02.

Zi JW, Cawood PA, Fan WM, Wang YJ, Tohver E, McCuaig TC, Peng TP. 2012a. Triassic collision in the Paleo-Tethys Ocean constrained by volcanic activity in SW China. Lithos, 144–145, 145–160. doi: 10.1016/j.lithos.2012.04.020.

Zi JW, Cawood PA, Fan WM, Wang YJ, Tohver E. 2012b. Contrasting rift and subduction-related plagiogranites in the Jinshajiang ophiolitic mélange, southwest China and implications for the Paleo-Tethys. Tectonics, 31, 1–18. doi: 10.1029/2011TC002937.